Electrical properties and aging characteristic of Sb/Ga co-doped single-cation oxide SnO$_2$

Shuyan Zhang[1,3], Hong Zhang[1,3], Senlin Leng[2], Yaqiong Wen[1], Hanxiao Wang[1], and Zhicheng Li[1,3,*] (iD)

[1] School of Materials Science and Engineering, Central South University, Changsha 410083, China
[2] School of Material and Chemical Engineering, Tongren University, Tongren 554300, China
[3] Hunan Key Laboratory of Electronic Packaging and Advanced Functional Materials, Central South University, Changsha 410083, China

ABSTRACT

A system of negative temperature coefficient (NTC) thermistors with adjustable room-temperature resistivity (ρ_{25}) and temperature sensitivity should have great application prospect for various requirements. Herein, Sb/Ga co-doped SnO$_2$ ceramics with nominal formula of Sn$_{0.95-x}$Sb$_{0.05}$Ga$_x$O$_2$ (x = 0, 0.01, 0.02, 0.03, 0.04, and 0.05) were fabricated by conventional solid-state reaction process. The phase component, electrical conductivity, temperature sensitivity of resistivity and aging characteristic were investigated. Analysis of X-ray diffraction shows that the prepared SnO$_2$-based ceramics consist of tetragonal phase. The ceramics exhibit typical characteristic of NTC of resistivity. With change of Ga-ion content, the ceramics possess adjustable ρ_{25} from 3.24 Ω·cm to 0.54 MΩ·cm together with related NTC material constants ($B_{25/85}$ values) from 140 to 5384 K. The analysis of complex impedance spectra reveals that both band conduction and hopping conduction are responsible for electrical properties of the prepared ceramics. The aging treatment induced at 150 °C revealed that all ceramics exhibit good electrical stability. The possible aging models were investigated by analysis of the change of element valences before and after aging.

1 Introduction

Typical negative temperature coefficient (NTC) thermistors exhibit the feature that the resistivity decreases exponentially with the increase of temperature, and possess the characteristics of high temperature sensitivity, good reliability, and quick response. NTC ceramic thermistors are widely applied in the regions of automobile, therapy, communication, computer, and other occasions, mainly playing a role in the suppression of surge current, overload protection, temperature measurement, and control and so on. The commonly applied materials for normal temperature NTC thermistors are the ones

based on spinel transition metal oxides, such as Mn–Co–Ni–O [1], Co–Mn–O [2], Ni–Mn–O [3, 4], etc. ABO$_3$-type perovskite compounds such as LaCrO$_3$ [5, 6], BaTiO$_3$ [7], and BaBiO$_3$ [8] are also regarded as the potential candidate for NTC thermistors. On the other hand, NTC thermistors based on single-cation oxides such as SnO$_2$, NiO, CuO, and ZnO have been recently reported for their unique feature that the room-temperature resistivity (ρ_{25}) and NTC material constant ($B_{25/85}$ value) can be effectively adjusted by changing the content and element type of solid solution ions [9–13]. For example, Li et al. reported that Al/La/Cu-modified ZnO-based ceramics have wide range of adjustable ρ_{25} and $B_{25/85}$ values of 0.65–3280 kΩ·cm and 2500–5850 K, respectively [12]. Yang et al. prepared B^{3+}/Na$^+$-modified NiO-based ceramics with adjustable ρ_{25} from 47.94 Ω·cm to 1.024 MΩ·cm and $B_{25/85}$ values from 2582 to 8019 K [10].

In the meanwhile, the electrical stability of NTC thermistors has recently attracted attention for its essential factor guaranteeing the reliability in practical application. Several models have been proposed to reveal the aging characteristics of NTC thermistors [14–20]. The change of resistance during aging treatment might be attributed to contact degradation, redistribution of cations over sublattices, and oxidation or reduction of oxygen, etc. [15]. In order to improve the aging stability, as reported by Li et al. [16], Na$^+$ cations were added into Mn$_{1.95}$Co$_{0.21}$Ni$_{0.84}$O$_4$, and clustered at grain boundary to hinder the transportation of oxygen vacancies. Ren et al. investigated the aging performance of Zn–Fe–Mn–Co–O spinel-structured thermistor films at different temperatures and found that high annealing temperature can enhance the aging performance due to the improved microstructure and density of films [17]. Gao et al. studied the influence of Bi$_2$O$_3$ on electrical stability of Na-doped Zn$_{0.4}$Ni$_{0.6}$O ((Zn$_{0.4}$Ni$_{0.6}$)$_{1-x}$Na$_x$O) NTC ceramics, and found that Bi$_2$O$_3$ can effectively enhance aging stability of the thermistors [18]. The Bi$_2$O$_3$-rich region in ceramics provides electrons for oxygen molecules that were adsorbed by ceramic during aging process, and depresses the redox reaction of the ceramics and aging deterioration.

SnO$_2$-based ceramics show potential candidate of NTC thermistor for their obvious advantage with effectively adjustable ρ_{25} and $B_{25/85}$ value in wide range by changing the dopant content, but the understanding of aging characteristics of SnO$_2$-based NTC ceramics is still insufficient. In present work, Sb/Ga co-doped SnO$_2$ ceramics were fabricated for NTC thermistors, the related electrical properties and aging characteristic were investigated. Combined with XPS analysis, moisture adsorption and related redox reaction were proposed for the mechanism of the aging-induced resistance shift of the SnO$_2$ ceramics.

2 Experimental

2.1 Sample preparation

According to the reported work on Sb-doped SnO$_2$ ceramics, the ceramic resistivity shows the smallest one when the doping content Sb is 5% (in molar percentage) [9, 21, 22]. The related nominal formula of ceramic with the smallest resistivity can be defined as Sn$_{0.95-x}$Sb$_{0.05}$O$_2$. Here, the influence of Ga-ionic content on the electrical performance of Sn$_{0.95}$Sb$_{0.05}$O$_2$ is carried out. Solid-state reaction process was used to prepared powders with nominal formula of Sn$_{0.95-x}$Sb$_{0.05}$Ga$_x$O$_2$ (denoted as SSGOx, x = 0, 0.01, 0.02, 0.03, 0.04 and 0.05), and the related ceramics were received by traditional sintering mothed. Raw materials of SnO$_2$ (99.5%, Xilong Scientific Co., Ltd., China), Sb$_2$O$_3$ (99%, Xilong Scientific Co., Ltd., China), and Ga$_2$O$_3$ (99.99%, Shanghai Longjin Metal Material Co., Ltd., China) powders were weighed according to the nominal formula. The raw materials were mixed by ball milling for 1 h with deionized water as dispersion agent and then were dried in an oven at 110 °C for 12 h. The dried mixtures were calcined at 800 °C for 5 h in air. Then 1% (in weight percentage) CuO (99%, Shanghai Macklin Biochemical Co., Ltd., China) was mixed with the calcined powders to promote sintering ability. The mixed powders were fully ground and granulated with solution of polyvinyl alcohol (PVA) in deionized water. Then the granulated powders were pressed into pellets with 12 mm in diameter and around 2 mm in thickness. The green pellets were sintered at 1350 °C for 1 h to get dense ceramics. The as-sintered ceramics were polished and coated with silver on both opposite sides, followed by being heated at 600 °C for 5 min to make ohmic electrodes for measuring electrical properties.

2.2 Characterization

The phase component and lattice parameters of as-sintered ceramics were characterized by X-ray diffractometer (XRD, Rigaku D/max 2500, Japan) with Cu Kα radiation with wavelength λ of 0.154056 nm. A scanning electron microscopy (SEM, JMS-7900 F) was employed to observe the microstructure of samples, and element distribution characterization was performed by an energy dispersive X-ray spectroscopy (EDS, Oxford Ultim Max 65). The ceramics used for SEM characterization were polished, followed by thermal etching at 1200 °C for 30 min. The valence states of elements in ceramics were analyzed by X-ray photoelectron spectroscopy (XPS, K-alpha 1063, UK). The relative densities of ceramics were received with the Archimedes method.

In order to investigate the electrical properties of SSGOx ceramics, a resistance–temperature measurement system (ZWX-C, Huazhong University of Science and Technology, China) was used to measure the resistances over temperature range between 25 and 250 °C. Alternating current (AC) impedance spectroscopy was implemented using an electrochemical workstation (Gamry Reference 600, USA) in frequency range from 1 Hz to 1 MHz, and the impedance spectra were analyzed with Gamry Echem Analyst.

Aging treatment was carried out to investigate the electrical stability of ceramics. The ceramics with ohmic electrodes were put into an oven which was held at 150 °C in air. After different aging periods, the samples were taken out from the oven and placed at room temperature for at least 60 min. Then the sample resistances were measured using FLUKE 8808A. The aging-induced resistance change rate $\Delta R/R_0$ was calculated by $\Delta R/R_0 = (R - R_0)/R_0$, where R_0 represents initial resistance of sample at 25 °C and R is sample resistance at 25 °C after being aged for some time.

3 Results and discussion

3.1 Phase and microstructure

Figure 1 illustrates SEM images of SSGO0 and SSGO0.04 ceramics. Dense ceramics are obtained, although few pores are present. The relative densities of SSGOx ceramics measured by Archimedes method are 98.8%, 96.9%, 95.6%, 95.2%, 92.7%, and 91.5% for x are 0, 0.01, 0.02, 0.03, 0.04, and 0.05, respectively. As can be seen in Fig. 1, there are two kinds of particles with different size. The particles with smaller size are distributed at the grain boundaries of the larger grains.

In order to figure out the composition distribution of different kinds of particles as shown in Fig. 1, EDS analysis was conducted for sample SSGO0.04. Figure 2 shows a SEM image and related EDS mapping of elemental distribution of thermally etched surface of SSGO4 ceramic.

The Sn element is uniformly distributed in the larger-sized particles, as shown in Fig. 2b. The Sb and Ga elements, as shown in Fig. 2c, d, are mainly distributed in the larger-sized particles, but a trace amount of them distribute in the smaller-sized particles. In the smaller-sized particles, Cu and O are the main elements (as shown in Fig. 2e, f). These indicate that the smaller-sized particles as shown in Fig. 1 are CuO-rich regions. CuO was introduced into the calcined SSGO powders as a sintering aid. Due to the low melting point of CuO (1026 °C) [12], a liquid phase was formed during the sintering process and distributed on the surface of the SSGO particles, which promoted the migration of substances and improved the ceramic density. At the same time, trace amounts of Sb and Ga that were not completely dissolved into SnO_2 lattice might form solid solutions or mixtures with CuO and locate at grain boundaries. So the CuO-rich liquid-like phase was distributed at the grain boundaries [23].

The XRD patterns of $Sn_{0.95-x}Sb_{0.05}Ga_xO_2$ ($x = 0$, 0.04, and 0.05) ceramics are shown in Fig. 3a. All the XRD patterns can be indexed as that of tetragonal SnO_2 crystal with a space group of $P4_2/mnm$ (Ref. PDF No. 99-0024). Combining with the elemental distribution in Fig. 2, it can be concluded that most of Sb ions and Ga ions had entered the lattice of SnO_2, substituted at the Sn sites and formed a solid solution with SnO_2. In addition, CuO-rich phase is present in ceramics, but there is no corresponding peak in the XRD patterns. It may be attributed to the detection limit of the X-ray diffractometer because the addition of CuO is only 1% in weight percentage, not enough to be detected by XRD.

Figure 3b is the partially magnified view of XRD patterns of (110) peak as shown in Fig. 3a. One can see that the (110) peak gradually shifts towards higher diffraction angle with the increase of Ga ions

Fig. 1 SEM images of thermally etched surface of $Sn_{0.95-x}Sb_{0.05}Ga_xO_2$ ceramics, **a** $x = 0$ SSGO0, and **b** $x = 0.04$ SSGO0.04
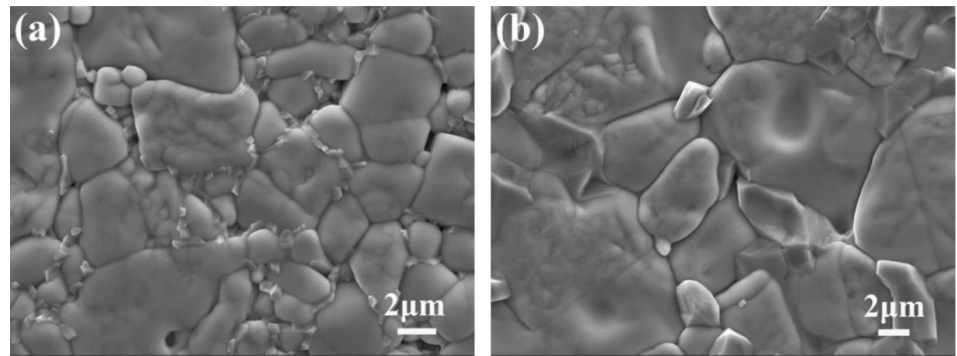
Fig. 2 EDS analysis of elemental distributions in SSGO0.04 ceramic, **a** SEM secondary electron image, **b** Sn element mapping, **c** Sb element mapping, **d** O element mapping, **e** Ga element mapping, and **f** Cu element mapping
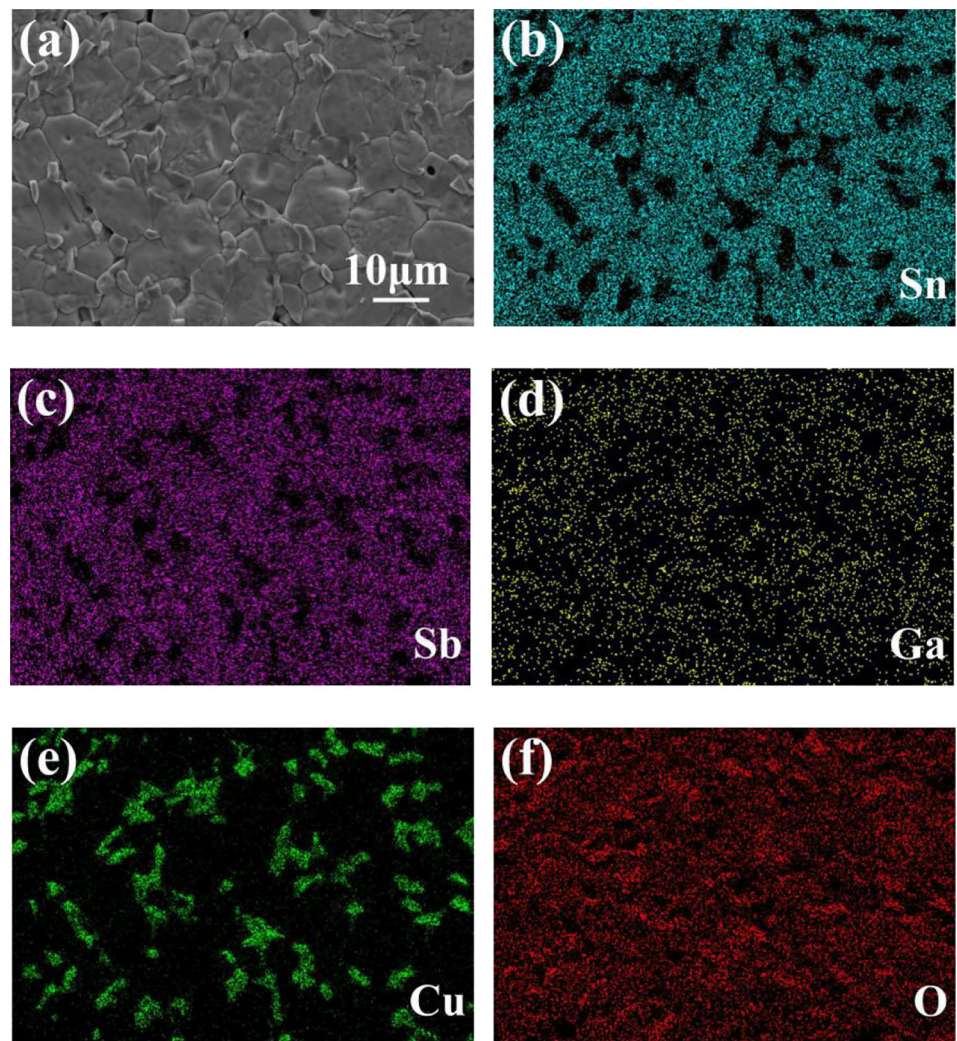
content, indicating that the interplanar spacing decreases. Lattice parameters and unit cell volumes of the measured ceramics are refined by Jade 6.5+ and listed in Table 1. The lattice parameters (a and c) and cell volumes decrease with the rise of Ga content. This is because that Ga^{3+} ions have been dissolved into SnO_2 lattice and the ionic radius of Ga^{3+} ions

(0.062 nm, in 6 coordination state) is smaller than that of Sn^{4+} ions (0.069 nm, in 6 coordination state) [24]. The substitution of Ga^{3+} ion at Sn^{4+}-ion site induced the lattice distortion and shrinking. At the same time, substitution of Ga^{3+} ions would produce oxygen vacancies as shown in defect reaction equation of Eq. (1). The occurrence of oxygen vacancies leads to

Fig. 3 Analysis of XRD patterns of as-sintered $Sn_{0.95-x}Sb_{0.05}Ga_xO_2$ (x = 0, 0.04, 0.05) ceramics, **a** whole XRD patterns, **b** partially magnified (110) peak, and **c** relationship between the cell volume and Ga content
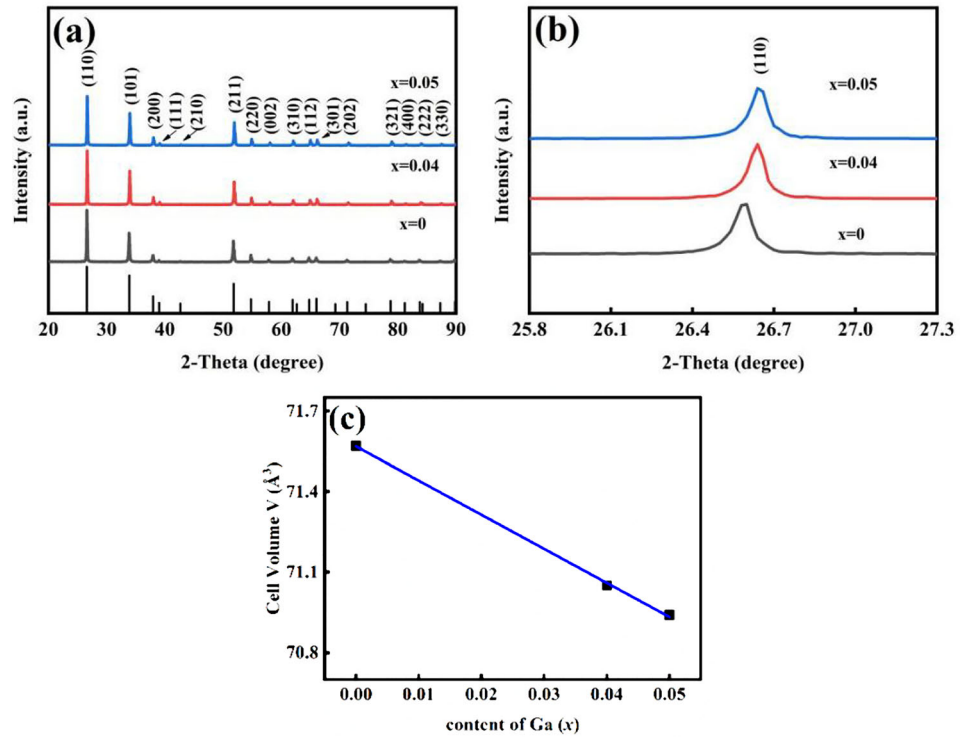
Table 1 Calculated lattice parameters and cell volumes of as-sintered $Sn_{0.95-x}Sb_{0.05}Ga_xO_2$ ceramics

x	Lattice parameter			Cell volume (nm³)
	a (nm)	b (nm)	c (nm)	
0	0.4737	0.4737	0.3189	0.0716
0.04	0.4728	0.4728	0.3178	0.0711
0.05	0.4727	0.4727	0.3156	0.0709

distortion and shrinking of related oxygen octahedrons, resulting in a reduction of lattice parameters.

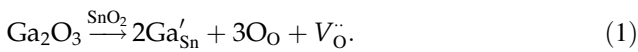$$Ga_2O_3 \xrightarrow{SnO_2} 2Ga'_{Sn} + 3O_O + V^{\cdot\cdot}_O. \tag{1}$$

Figure 3c presents the relationship between the cell volume and x, namely the concentration of Ga^{3+}. When x increases, the unit cell volume decreases linearly. According to Kostikova's research on Vegard law, this linear relationship further proves the presence of solid solution [6].

3.2 Electrical properties

The resistance changes with temperature of $Sn_{0.95-x-}Sb_{0.05}Ga_xO_2$ (x = 0, 0.01, 0.02, 0.03, 0.04, 0.05) were measured using a resistance–temperature measurement system over the temperature range from room

temperature to 250 °C. The corresponding resistivity was calculated according to formula of $\rho = RS/l$, where R is measured resistance, S is cross-sectional area of the circular ceramic sample, and l is the thickness of the sample perpendicular to the cross section. The plots of temperature dependence of resistivity ($\ln\rho$–$1000/T$) of SSGOx ceramics are shown in Fig. 4a. All SSGOx ceramics possess typical NTC characteristics, and the plot of $\ln\rho$–$1000/T$ for each sample has an approximate linear relationship. The relationship between $\ln\rho$ and $1000/T$ obeys the Arrhenius law as shown in Eq. (2).

$$\rho = A\exp\left(\frac{E_a}{kT}\right) = A\exp\left(\frac{B}{T}\right), \tag{2}$$

where ρ is resistivity at absolute temperature T, A is a constant relevant to material characteristic, E_a is activation energy of conduction, k is the Boltzmann

Fig. 4 Electrical properties of SSGOx ceramics, **a** $\ln\rho$–1000/T plots, and **b** Ga concentration dependence of ρ_{25} and $B_{25/85}$
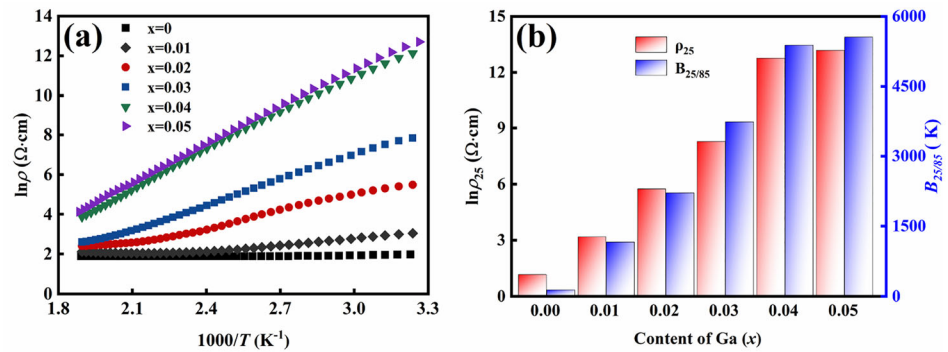

constant (which is 1.38×10^{-23} J/K), and B is NTC material constant reflecting the temperature sensitivity of a NTC thermistor. For NTC thermistors, B value can be calculated according to Eq. (3).

$$B_{25/85} = \frac{\ln\rho_{25} - \ln\rho_{85}}{1/T_{25} - 1/T_{85}}, \quad (3)$$

where ρ_{25} and ρ_{85} are resistivity at 25 °C (298 K) and 85 °C (358 K), respectively. So the B value is often denoted as $B_{25/85}$.

Figure 4b shows plots of ρ_{25} and $B_{25/85}$ as a function of Ga concentration in SSGOx ceramics. The ρ_{25} of SSGOx are 3.2 Ω·cm, 24 Ω·cm, 3.15×10^2 Ω·cm, 4×10^3 Ω·cm, 3.5×10^5 Ω·cm, and 5.3×10^5 Ω·cm for x are 0, 0.01, 0.02, 0.03, 0.04, and 0.05, respectively. The related $B_{25/85}$ are 140 K, 1161 K, 2214 K, 3735 K, 5384 K, and 5560 K, individually. With the increase of Ga content, both ρ_{25} and $B_{25/85}$ increase.

Generally, the substitution of heterovalent ions into a crystal may induce the occurrence of point defects and charge carriers. When higher valent ion donors are introduced, positively charged point defects and electrons will be generated, and the produced electrons may be excited to the conduction band of the semiconductor to form electron carriers. Negatively charged point defects and holes are generated when a crystal is doped with lower-valent ion acceptor, and holes may be excited from the acceptor energy level to the valence band, thus, playing the role of conduction. In the experiment, Sb_2O_3 was selected as the starting material, and Sb_2O_3 can be easily oxidized to Sb_2O_5 during calcination and sintering [25]. In SSGO system, both donor and acceptor doping are introduced into SnO_2 crystal lattice, in which Sb^{5+} acts as donor, Ga^{3+} and Sb^{3+} ions act as acceptors. For the doping of Sb^{5+} ions into SnO_2 lattice, defect reaction may take place as shown in Eq. (4).

$$Sb_2O_5 \xrightarrow{SnO_2} 2Sb_{Sn}^{\cdot} + 4O_O + 2e' + \frac{1}{2}O_2. \quad (4)$$
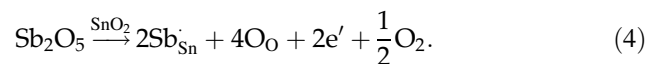
Here, Sb_2O_5 acts as a donor and produces weakly bound electron carriers, thereby enhancing the conductivity of the ceramics. These electrons are located in the donor energy level, which is closer to the conduction band than the valence band, so the electrons can be excited to the conduction band more easily. The activation energy required for electron conduction is reduced, and the material constant $B_{25/85}$ decreases.

When Ga^{3+} ion dops into SnO_2, Ga^{3+} replaces Sn^{4+} ions to generate holes, the related defect reaction is shown in Eq. (5).

$$Ga_2O_3 + \frac{1}{2}O_2 \xrightarrow{SnO_2} 2Ga'_{Sn} + 4O_O + 2h^{\cdot}. \quad (5)$$
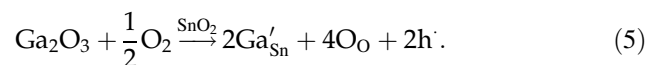
The holes react with electrons generated by Sb^{5+} doping to form electron–hole pair, or the electrons in conduction band (or donor level) transition to valence band (or acceptor level) to recombine with holes. Those processes reduce the concentration of electron charge carriers shown in Eq. (4). Therefore, the resistivity increases with the rise of Ga concentration.

As shown in Eq. (1), the substitution of Ga^{3+} ions at Sn^{4+} sites induced the formation of oxygen vacancies, and resulted in lattice distortion and increase of location lattice potential. So the charge carriers need more energy to transfer the lattice-distorted regions, indicating that the activation energy of conduction inside grains (E_g) is bigger in Ga-doped ceramics than in the undoped one. At the same time, for the different valences between Ga^{3+} and Sn^{4+} ions, the increase of Ga-ion content might exceed the solid solution limit of Ga_2O_3 in SnO_2, and results in the occurrence of impurity locating at grain

boundaries. The impurity should be composed of various elements such as Sb-, Ga-, and Cu-ions, and is always poor conductor to the charge carriers (electron or hole). As a result, the potential barrier of grain boundary increases with the increase of Ga-ion content. So the charge carriers transfer over the grain boundaries must overcome higher potential, resulting in higher activation energy of conduction at grain boundaries (E_{gb}). The total activation energy of conduction (E_a) is composed of E_g and E_{gb}, e.g., $E_a = E_g + E_{gb}$. Therefore, the higher concentration of Ga ions is, the higher E_a is. According to Eq. (2), the material constant B is proportional to E_a, so the $B_{25/85}$ value increases with increasing Ga concentration.

Table 2 shows comparison of electrical properties of $Sn_{0.95-x}Sb_{0.05}Ga_xO_2$ and some published NTC materials. Both ρ_{25} and $B_{25/85}$ of $Sn_{0.95-x}Sb_{0.05}Ga_xO_2$ can be adjusted in a wider range only by changing the concentration of Ga^{3+}-ions and have obviously larger adjustable regions than those in perovskite or spinel compounds. These indicate that the system of Ga-doped $Sn_{0.95}–Sb_{0.05}O_2$ ($Sn_{0.95-x}Sb_{0.05}Ga_xO_2$) NTC thermistors have potential wide application prospect to actual requirements.

3.3 AC impedance analysis

To further analyze the reason for the Ga content on the resistances of ceramics, AC impedance test was performed on SSGOx (x = 0.02, 0.03, 0.04, 0.05) at room temperature. The impedance Z^* can be described by $Z^* = Z' + jZ''$, where Z' is real part of impedance, and Z'' is imaginary part of impedance. The impedance in Nyquist plots are shown in Fig. 5a, b. The impedance in Nyquist plot of ideal polycrystal consists of two semicircles, corresponding to grain and grain boundary, respectively. Only one depressed semicircle can be observed in Fig. 5, because the

arcs of the grain and grain boundary overlap. In order to reveal the characteristic of the complex impedance spectra, an equivalent circuit as the inset in Fig. 5a was selected to fit the spectra. R_1 and R_2 represent resistances from grain effect and grain boundary effect, respectively, C_1 and C_2 are respective capacitance of grain effect and grain boundary effect, and CPE1 and CPE2 are constant phase elements. It can be seen that the fitting results are in good agreement with the measured data. The Ga concentration dependence of fitted resistances of grain effect and grain boundary effect is shown in Fig. 5c. With the increase of Ga content, both the resistances of grain effect and grain boundary effect simultaneously increase. The increase of grain resistance results from more holes generated with the increase of Ga content, as shown in the defect reaction in Eq. (5). The recombination of electrons and generated holes reduces the amount of carriers (electrons) in the grain, thereby increasing the grain resistance.

The increase of grain boundary resistance with Ga addition should be attributed to the variation of grain boundary barrier. When charge carriers cross grain boundary, they should overcome grain boundary barrier (E_{gb}). According to the Boltzmann statistical distribution law, the probability for a charge carrier to reach E_{gb} is proportional to $\exp(-E_{gb}/kT)$, meaning that the chance to overcome the barrier is exponentially relevant to E_{gb}. For the limited solid solubility of Sb/Ga in SnO_2, impurity must form when the content of dopants (Sb and Ga ions) is high enough. With the increase of Ga-ion content, more impurity might occur and locate at grain boundaries. The impurity should be composed of various elements such as Sb, Ga, and Cu ions and is always poor conductor to the charge carriers (electron or hole). As a result, the potential barrier of grain boundary

Table 2 Comparison of electrical properties of different NTC thermistors

NTC thermistors	ρ_{25}	$B_{25/85}$	References
$LaCr_{1-x}Mn_xO_3$ ($0 \leq x \leq 0.7$)	15.0–51,505.3 Ω·cm	3191–4301 K	[6]
$Sn_{0.95-y}Sb_{0.05}Cr_yO_2$ ($0 \leq y \leq 0.5$)	4.9 Ω·cm–16 MΩ·cm	149–4289 K	[9]
$Zn_{1-x}Sb_xO$ ($0 \leq x \leq 0.025$)	57.18 kΩ·cm–2.59 MΩ·cm	2284–4754 K	[13]
$Ni_{0.6}Mn_{2.4-x}Sn_xO_4$ ($0 \leq x \leq 0.5$)	5920 Ω·cm–5 MΩ·cm	3993–5100 K	[26]
$Ni_{0.5}Co_{0.5}Zn_xMn_{2-x}O_4$ ($0.15 \leq x \leq 0.3$)	2305–2475 Ω·cm	3640–3660 K	[27]
$Sn_{0.95-x}Sb_{0.05}Ga_xO_2$ ($0 \leq x \leq 0.5$)	3.24 Ω·cm–0.54 MΩ·cm	140–5384 K	This work

Fig. 5 Analysis of complex impedance spectra of SSGOx ceramics, measured at room temperature, **a** Nyquist plots of SSGOx (x = 0.02, 0.03), the inset shows the equivalent fitting circuit, **b** Nyquist plots of SSGOx (x = 0.04, 0.05), and **c** Ga concentration dependence of resistances of grain and grain boundary effect
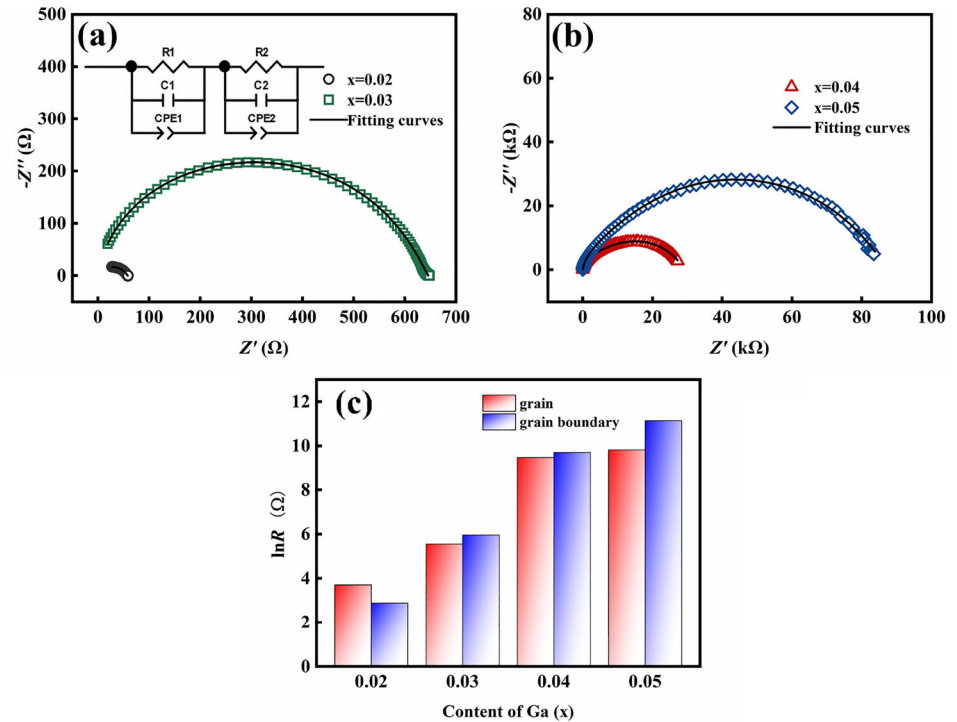
increases. So it is more difficult for carriers to transition at grain boundary, leading to higher grain boundary resistance and E_{gb}.

In order to figure out the conduction mechanism of SSGOx ceramics, analysis of SSGO0.04 sample's impedance spectra recorded at different temperatures was performed. Figure 6a, b is the Nyquist plots of the SSGO0.04 sample at different temperatures. The measured impedance spectra were fitted using the inset in Fig. 5a as the equivalent circuit. The fitting results are in good agreement with the measured impedance spectra. As shown in Fig. 6c, the fitted grain, grain boundary, and total resistances decrease with increasing temperature, consistent with the analysis of Fig. 4a, confirming the NTC characteristic of the ceramics. The corresponding activation energy was acquired according to Eq. (2), which has been marked in Fig. 6c. The activation energies of grain effect and grain boundary effect are 0.41 eV and 0.32 eV, respectively. This indicates that the electrical behavior of the ceramics is affected by both grain effect and grain boundary effect.

Figure 6d is plots of frequency dependence of the normalized imaginary part of impedance (Z''/Z''_{max}). The relationship between Z'' and frequency follows

$$Z'' = \omega\tau R/(1 + (\omega\tau)^2),$$

where ω is angular frequency, τ is time constant, and

R is resistance. When Z'' reaches a maximum value, the corresponding

$$\tau = 1/\omega_c = 1/(2\pi f_c),$$

where ω_c is characteristic angular frequency and f_c is characteristic frequency. It can be seen from Fig. 6d that with the increase of temperature, f_c gradually increases and the time constant decreases, indicating the existence of thermally activated conduction.

The admittance (σ) is inversely proportional to impedance (Z) with the relationship of $\sigma = 1/Z$. The real part of σ obeys the Jonscher's power law [14]:

$$\sigma'(\omega) = \sigma'(0) + D\omega^n, \tag{6}$$

where $\sigma'(\omega)$ represents real part of conductivity, ω is angular frequency, and $\sigma'(0)$ is the DC conductivity which can be extracted from the value of $\sigma'(\omega)$ when ω approaches to zero, D is a constant related to temperature. n is power exponent that depends on temperature and material characteristic ranging from 0 to 1. The relationship of $\log\sigma'(\omega)$ and $\log\omega$ is illustrated in Fig. 6e. The $\sigma'(\omega)$ is frequency independent in lower-frequency region, but increases with frequency in higher-frequency region after a critical point. The variation of $\sigma'(\omega)$ with frequency indicates that in addition to band conduction, there is another frequency-dependent conduction mechanism. Figure 6f shows the relationship between $\log[\sigma'(\omega) -$

Fig. 6 Analysis of impedance spectra of $Sn_{0.91}Sb_{0.05}Ga_{0.04}O_2$ ceramic measured at various temperatures, **a** and **b** Nyquist plots at different temperatures, **c** temperature dependence of R_g, R_{gb}, and $R_g + R_{gb}$, **d** plots for frequency dependence of the imaginary impedance part Z'', **e** angular frequency ω dependence of complex conductivity $\sigma'(\omega)$, and **f** $\log[\sigma'(\omega) - \sigma'(0)]$– $\log\omega$ plots
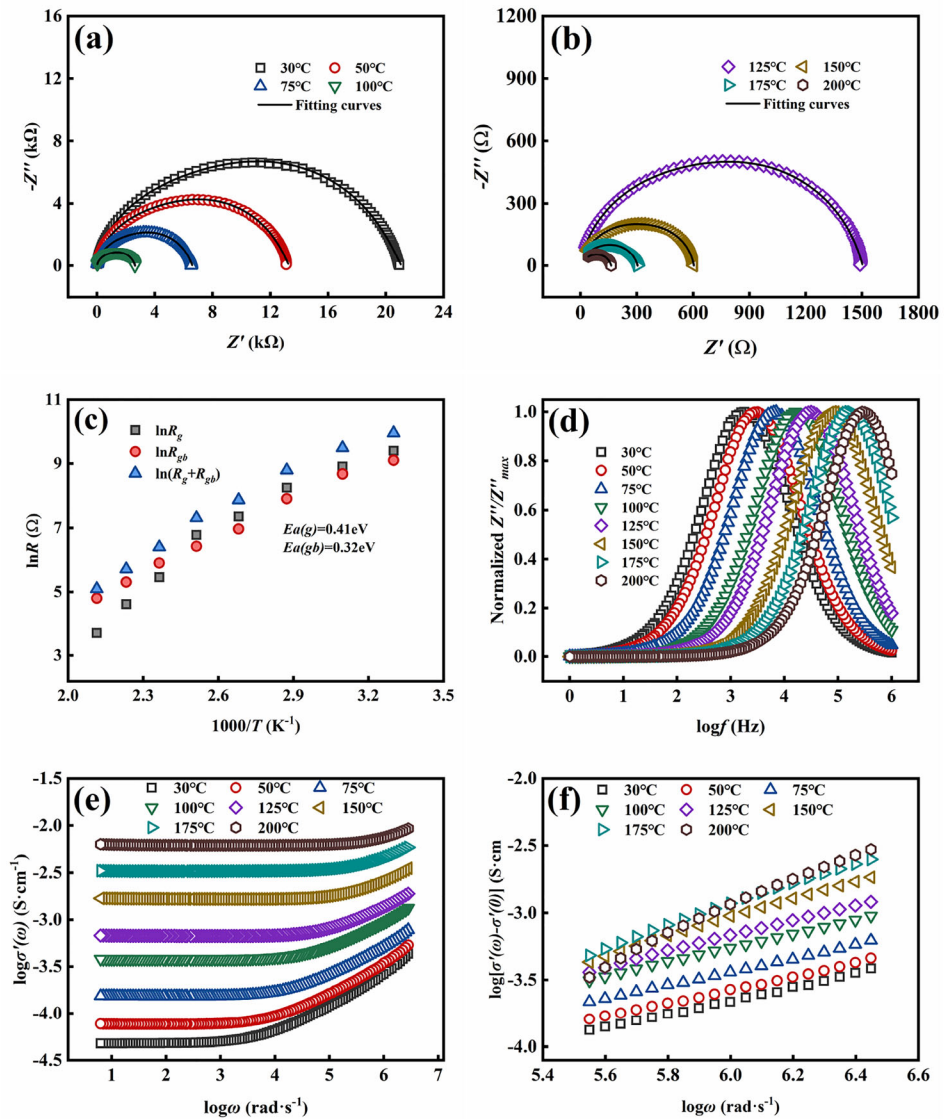
$\sigma'(0)]$ and $\log\omega$. n can be obtained by calculating the slope of the fitting lines. The values of n are 0.5778, 0.5654, 0.5508, 0.5534, 0.5870, 0.6818, 0.7625, and 0.9712 at temperatures of 30, 50, 75, 100, 125, 150, 175, and 200 °C, respectively. The n values are less than 1 at all temperatures, indicating the presence of hopping conduction assisted by small polaron hopping mechanism at higher frequency [28]. In $Sn_{0.95-x}$-$Sb_{0.05}Ga_xO_2$ system, Sb ions possess both + 3 and + 5 valences. The virtual Sb^{4+} is proposed to explain the hopping behavior between Sb^{3+} and Sb^{5+} [29]. The mechanism of hopping conduction can be expressed by Eq. (7).

$$Sb^{3+} + Sb^{5+} \leftrightarrow 2Sb^{4+} \leftrightarrow Sb^{5+} + Sb^{3+}. \tag{7}$$
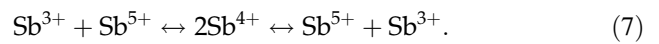
As discussed above, band conduction and hopping conduction simultaneously act on the conduction behavior of SSGOx ceramics.

3.4 Ageing properties

The variation of resistance change rates ($\Delta R/R_0$) of SSGOx ($x = 0, 0.01, 0.02, 0.03, 0.04, 0.05$) ceramics during aging process are presented in Fig. 7a. It indicates that the resistances of all samples decreased slightly with increasing of aging time. And the absolute values of $\Delta R/R_0$ increased as the concentration of Ga in SSGOx increases. After 500 h of aging

Fig. 7 Aging properties of SSGO ceramics, **a** relationship between $\Delta R/R_0$ and aging time for SSGOx ($x = 0$–0.05) samples, and **b** impedance spectra in Nyquist plots of SSGO0.04 ceramic before and after aging
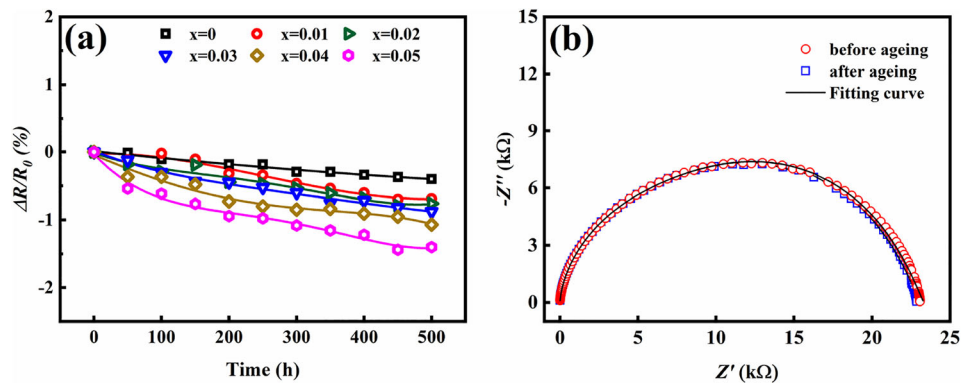
treatment at 150 °C, the $\Delta R/R_0$ values of SSGOx are $- 0.40\%$ ($x = 0$), -0.69% ($x = 0.01$), $- 0.76\%$ ($x = 0.02$), $- 0.88\%$ ($x = 0.03$), $- 1.02\%$ ($x = 0.04$), and $- 1.40\%$ ($x = 0.05$).

To investigate the variation of grain effect and grain boundary effect induced by aging, AC impedance analysis for the same SSGO0.04 sample was conducted before and after aging. The results are shown in Fig. 7b. The equivalent circuit as the inset one in Fig. 5a was selected. The fitted grain resistances before and after aging are 10,326 and 10,189 Ω, respectively. The fitted grain boundary resistances before and after aging are 13,005 and 12,903 Ω, respectively. Both resistances of grain effect and grain boundary effect decreased after aging. The total resistance change rate is $- 1.02\%$. The resistance change rates of grain and the grain boundary are $- 1.38\%$ and $- 0.78\%$, indicating that the change of ceramic resistance results from both the grain and grain boundary, and the grain plays the main role.

Figure 8 shows the comparative XPS analysis of SSGO0 and SSGO0.04 ceramics before and after aging. Figure 8a and b are narrow spectra of Sn element in SSGO0 and SSGO0.04 ceramics, respectively, before and after aging. Sn element has only a $+ 4$ valence state in all samples, and there is no change in valence state before and after aging.

In Fig. 8c (for SSGO0) and 8d (for SSGO0.04), each Sb 3d$_{3/2}$ XPS spectrum can be divided into two peaks. The peak locates between 537.7 eV and 538.8 eV corresponds to Sb^{3+} and the one between 540.4 eV and 540.6 eV corresponds to Sb^{5+}. Compared the areas of fitted peaks, the content ratios of Sb^{5+} to Sb^{3+} ions (denoted as [Sb^{5+}]/[Sb^{3+}]) changed from 0.31 to 0.29 for SSGO0 ceramic and from 0.58 to 0.38 for SSGO0.04 ceramic. The [Sb^{5+}]/[Sb^{3+}] in both ceramics decreased after aging.

Figure 8e and f is narrow spectra of Cu element before and after aging in SSGO0 and SSGO0.04 samples, respectively. The peaks located at 932.4 eV and 952.2 eV correspond to 2p$_{1/2}$ and 2p$_{3/2}$ peaks of Cu$^+$, respectively. The peaks at 933.7 eV and 953.9 eV correspond to 2p$_{1/2}$ and 2p$_{3/2}$ peaks of Cu^{2+}, respectively. And the peaks at 940.4 eV and 943.3 eV are satellite peaks of Cu^{2+}. The content ratio of Cu^{2+} and Cu$^+$ ions can be obtained by calculating the area ratio of related XPS peaks. For SSGO0 sample, the content ratio of Cu^{2+} and Cu$^+$ ions (denoted as [Cu^{2+}]/[Cu$^+$]) decreased from 0.99 to 0.83 after aging, while the one of [Cu^{2+}]/[Cu$^+$] in the SSGO0.04 sample decreased from 0.61 to 0.41.

Combined with the change of content ratios of [Sb^{5+}]/[Sb^{3+}] and [Cu^{2+}]/[Cu$^+$] before and after aging, one can get that the valence states of Sb ions and Cu ions had been reduced during the aging process. The decrease in resistance of the samples after aging should be due to the increase of electrons in the ceramics. The reason for the increase of electrons may be attributed to the adsorption and reaction of the moisture (water) during aging process. When the aging test was performed on the samples in the air, the moisture would be adsorbed on the surface of the ceramic and then react with the holes in the acceptor level generated by Ga^{3+} doping [13], as shown in Eqs. (8) and (9). Since holes were consumed by adsorbed water, more electrons would be generated in order to maintain electrical neutrality. Some of the electrons generated during aging reacted with Sb^{5+} to form Sb^{3+}, the others acted as carriers for conduction together with the original electrons. Consequently, not only the ratio of Sb^{5+}/Sb^{3+} reduced, but also the resistance of the ceramic decreased after aging due to the increase of carrier (electrons) concentration.

Fig. 8 Comparative analysis of XPS spectra for SSGO ceramics with and without Ga^{3+} ion, before and after aging, **a** Sn 3d spectra for SSGO0, **b** Sn 3d spectra for SSGO0.04, **c** Sb 3d spectra for SSGO0, **d** Sb 3d spectra for SSGO0.04, **e** Cu 2p spectra for SSGO0, and **f** Cu 2p spectra for SSGO0.04

$$h^{\cdot} + H_2O_{ads} \rightarrow HO^{\cdot} + H^+, \tag{8}$$

$$2h^{\cdot} + H_2O_{ads} \rightarrow \frac{1}{2}O_2 + 2H^+. \tag{9}$$
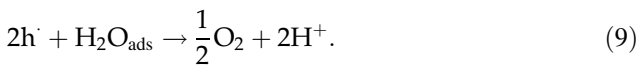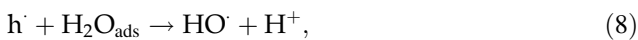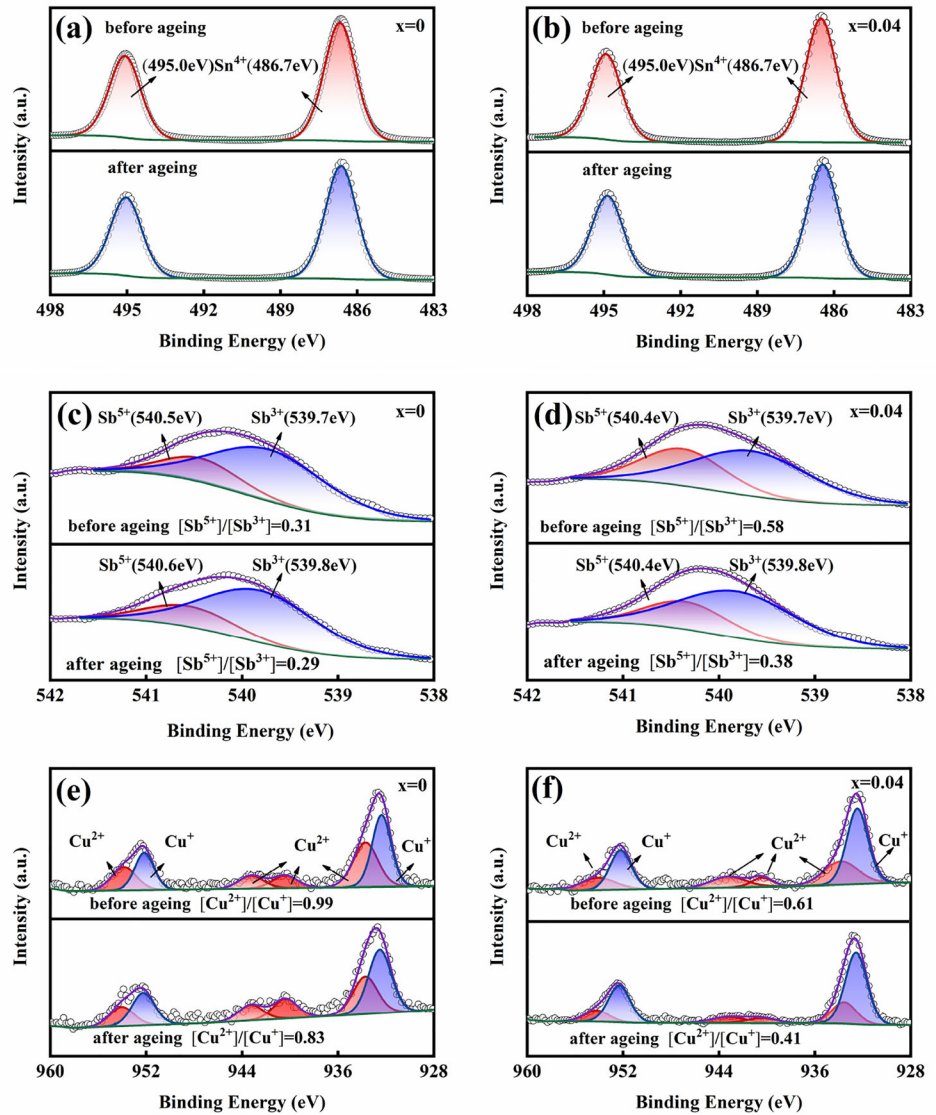
Similar to Sb ions, the change in the valence state of Cu ions is also due to the presence of more electrons in the ceramic, except that the electrons are mainly from the grain boundary. The water adsorbed on the ceramic surface reacted with the holes at the grain boundary, as shown in Eqs. (8) and (9). In order to maintain electrical neutrality, more electrons were generated, some of which reacted with Cu^{2+} to form Cu^+, the others acted as carriers. Therefore, the content ratio of Cu^{2+}/Cu^+ reduced, and the grain boundary resistance also decreased due to the

increase of carrier concentration. In addition, the ratio changes of Sb^{5+}/Sb^{3+} and Cu^{2+}/Cu^+ in SSGO0 are less than those in SSGO0.04, respectively, which is consistent with the resistance change rate of both samples.

Although the resistance of SSGO ceramic samples decreases after aging, the resistance change rate is less than − 1.4% for all samples, indicating that the samples have stable electrical properties.

4 Conclusion

$Sn_{0.95−x}Sb_{0.05}Ga_xO_2$ $(0 \leq x \leq 0.05)$ ceramics were synthesized with solid-state processes. All of the compositions exhibit typical NTC characteristic.

Changing the concentration of Ga ions can effectively adjust room-temperature resistivity from 3.24 Ω·cm to 0.54 MΩ·cm and temperature sensitivity (material constant B value) from 140 to 5384 K of the ceramics. The prepared NTC ceramics possess stable electric properties, the resistance change ratio $\Delta R/R_0$ is less than 1.4% even after being aged at 150 °C for 500 h. These make that the $Sn_{0.95-x}Sb_{0.05}Ga_xO_2$ NTC thermistors have potential application. Band conduction and hopping conduction are responsible for electrical properties of the ceramics. The adsorption and reaction of water in the air are the reason for the resistance change after aging.

Author contributions

ZL, HZ, and SZ contributed to the study conception and design. Material preparation, data collection, and analysis were performed by SZ, SL, YW, and HW. The first draft of the manuscript was written by SZ, and all authors commented on previous versions of the manuscript. All authors read and approved the final manuscript.

Funding

Data availability

The datasets generated during and/or analyzed during the current study are available from the corresponding author on reasonable request.

Declarations

Conflict of interest The authors have no relevant financial or non-financial interests to disclose.

References

1. L. Chen, W. Kong, J. Yao, B. Gao, Q. Zhang, H. Bu, A. Chang, C. Jiang, Effect of sintering temperature on microstructure and electrical properties of $Mn_{1.2}Co_{1.5}Ni_{0.3}O_4$ ceramic materials using nanoparticles by reverse microemulsion method. J. Mater. Sci. Mater. Electron. **27**, 1713–1718 (2015)

2. C. Ma, H. Gao, TEM and electrical properties characterizations of $Co_{0.98}Mn_{2.02}O_4$ NTC ceramic. J. Alloys Compd. **749**, 853–858 (2018)

3. R. Jadhav, D. Kulkarni, V. Puri, Structural and electrical properties of fritless $Ni_{(1-x)}Cu_xMn_2O_4$ (0 ≤ x ≤ 1) thick film NTC ceramic. J. Mater. Sci. Mater. Electron. **21**, 503–508 (2009)

4. J. Wang, J. Zhang, Structural and electrical properties of $NiMg_xMn_{2-x}O_4$ NTC thermistors prepared by using sol–gel derived powders. Mater. Sci. Eng. B **176**, 616–619 (2011)

5. P. Luo, B. Zhang, Q. Zhao, D. He, A. Chang, Characterization and electrical conductivity of $La_{1-x}Sr_xCrO_3$ NTC ceramics. J. Mater. Sci. Mater. Electron. **28**, 9265–9271 (2017)

6. F. Guan, Z. Dang, X. Chen, S. Huang, J. Wang, X. Cheng, Y. Wu, Novel electrical properties of Mn-doped $LaCrO_3$ ceramics as NTC thermistors. J. Alloys Compd. **871**, 159269 (2021)

7. Y. Luo, X. Liu, G. Chen, Electrical properties of $BaTiO_3$-based NTC thermistors doped by $BaBiO_3$ and CeO_2. J. Alloys Compd. **429**, 335–337 (2007)

8. J. Qu, S. Li, F. Liu, X. Liu, Z. Chen, C. Yuan, X. Liu, Y. Zhao, D. Zhou, Effect of phase structures and substrate temperatures on NTC characteristics of Cu-modified Ba–Bi–O-based perovskite-type thermistor thin films. Mater. Sci. Semicond. Process. **121**, 105375 (2021)

9. W. Yan, H. Zhang, X. Wang, C. You, Z. Li, Characterization of electrical conductivity and temperature sensitivity of Cr/Sb-modified SnO_2 ceramics. J. Mater. Sci. Mater. Electron. **31**, 4040–4049 (2020)

10. Z. Yang, H. Zhang, Z. He, B. Li, Z. Li, Influence of B^{3+}- and Na^+-ions on electrical property and temperature sensitivity of NiO-based ceramics. J. Mater. Sci. Mater. Electron. **30**, 3088–3097 (2019)

11. C. You, Z. Li, S. Zhang, G. Jiang, H. Zhang, Electrical properties of Sr-modified CuO ceramics. J. Mater. Sci. Mater. Electron. **32**, 15907–15916 (2021)

12. P. Li, H. Zhang, C. Gao, G. Jiang, Z. Li, Electrical property of Al/La/Cu modified ZnO-based negative temperature coefficient (NTC) ceramics with high ageing stability. J. Mater. Sci. Mater. Electron. **30**, 19598–19608 (2019)

13. B. Li, Z. Li, D. Peng, L. Huang, S. Zhang, H. Zhang, Sb-doped ZnO ceramics: NTC thermistors with high temperature

sensitivity and electrical stability. J. Mater. Sci. Mater. Electron. **32**, 24296–24307 (2021)

14. X. Sun, S. Leng, H. Zhang, Z. He, Z. Li, Electrical properties and temperature sensitivity of Li/Mg modified $Ni_{0.7}Zn_{0.3}O$ based ceramics. J. Alloys Compd. **763**, 975–982 (2018)

15. W.A. Groen, C. Metzmacher, V. Zaspalis, P. Huppertz, S. Schuurman, Aging of NTC ceramics in the system Mn–Ni–Fe–O. J. Eur. Ceram. Soc. **21**, 1793–1796 (2001)

16. H. Li, I.P.L. Thayil, X. Ma, X. Sang, H. Zhang, A. Chang, Electrical properties and aging behavior of Na-doped $Mn_{1.95}Co_{0.21}Ni_{0.84}O_4$ NTC ceramics. Ceram. Int. **46**, 24365–24370 (2020)

17. W. Ren, N. Zhu, L. Li, H. Feng, Y. Wang, Y. Yang, Z. Yang, S. Shang, Improvement of ageing issue in $Zn_{0.4}Fe_{2.1}Co_{2-}Mn_{1.5}O_8$ thermistor films. J. Eur. Ceram. Soc. **39**, 4189–4193 (2019)

18. C. Gao, Z. Li, L. Yang, D. Peng, H. Zhang, Investigation of electrical and aging properties of Bi-modified $(Zn_{0.4-}Ni_{0.6})_{1-x}Na_xO$ ceramic thermistors. J. Eur. Ceram. Soc. **41**, 4160–4166 (2021)

19. M.M. Vakiv, O.I. Shpotyuk, V.O. Balitska, B. Butkiewicz, L.I. Shpotyuk, Ageing behavior of electrical resistance in manganite NTC ceramics. J. Eur. Ceram. Soc. **24**, 1243–1246 (2004)

20. D. Fang, C. Zheng, C. Chen, A.J.A. Winnubst, Aging of nickel manganite NTC ceramics. J. Electroceram. **22**, 421–427 (2008)

21. G. Jiang, Z. Li, C. You, W. Hao, Z. Ma, H. Zhang, Temperature sensitivity and electrical stability of Sb/Mn co-doped SnO_2 ceramics. J. Mater. Sci. Mater. Electron. **32**, 16945–16955 (2021)

22. J. Zhang, H. Zhang, B. Yang, Y. Zhang, Z. Li, Temperature sensitivity of Fe-substituted SnO_2-based ceramics as negative temperature coefficient thermistors. J. Mater. Sci. Mater. Electron. **27**, 4935–4942 (2016)

23. T.S. Zhang, L.B. Kong, X.C. Song, Z.H. Du, W.Q. Xu, S. Li, Densification behaviour and sintering mechanisms of Cu- or Co-doped SnO_2: a comparative study. Acta Mater. **62**, 81–88 (2014)

24. R.D. Shannon, Revised effective ionic radii and systematic studies of interatomic distances in halides and chalcogenides. Acta Crystallogr. **32**, 751–767 (1976)

25. S. Gong, Z. Chen, F. Tang, P. Pi, X. Wen, Preparation and characterization of antimony doped tin oxide nanoparticles. J. Chin. Ceram. Soc. **37**, 648–652 (2009)

26. Z. Wang, Z. Li, Y. Zhang, R. Zhang, P. Qin, C. Chen, L. Winnubst, Preparation and electrical properties of $Ni_{0.6-}Mn_{2.4-x}Sn_xO_4$ NTC ceramics. Ceram. Int. **40**, 4875–4878 (2014)

27. B.Y. Price, G. Hardal, Preparation and characterization of Ni–Co–Zn–Mn–O negative temperature coefficient thermistors with B_2O_3 addition. J. Mater. Sci. Mater. Electron. **30**, 17432–17439 (2019)

28. R. Kaur, V. Sharma, M. Kumar, M. Singh, A. Singh, Conductivity relaxation in $Pb_{0.9}Sm_{0.10}Zr_{0.405}Ti_{0.495}Fe_{0.10}O_3$ solid solution. J. Alloys Compd. **735**, 1472–1479 (2018)

29. M.A.L. Nobre, S. Lanfredi, Dielectric spectroscopy on $Bi_{3-}Zn_2Sb_3O_{14}$ ceramic: an approach based on the complex impedance. J. Phys. Chem. Solids **64**, 2457–2464 (2003)